

# Geometric Constrained Non-Line-of-Sight Imaging

Xueying Liu, Lianfang Wang, Jun Liu, Yong Wang and Yuping Duan

**Abstract**—Normal reconstruction is crucial in non-line-of-sight (NLOS) imaging, as it provides key geometric and lighting information about hidden objects, which significantly improves reconstruction accuracy and scene understanding. However, jointly estimating normals and albedo expands the problem from matrix-valued functions to tensor-valued functions that substantially increasing complexity and computational difficulty. In this paper, we propose a novel joint albedo-surface reconstruction method, which utilizes the Frobenius norm of the shape operator to control the variation rate of the normal field. It is the first attempt to apply regularization methods to the reconstruction of surface normals for hidden objects. By improving the accuracy of the normal field, it enhances detail representation and achieves high-precision reconstruction of hidden object geometry. The proposed method demonstrates robustness and effectiveness on both synthetic and experimental datasets. On transient data captured within 15 seconds, our surface normal-regularized reconstruction model produces more accurate surfaces than recently proposed methods and is 30 times faster than the existing surface reconstruction approach.

**Index Terms**—Non-line-of-sight imaging, under-sampled scanning, surface normal, shape operator, surface regularization.

## I. INTRODUCTION

IN typical Non-Line-of-Sight (NLOS) imaging, a hidden target is detected through light scattered off a surface, which, while unclear, can now reveal hidden objects thanks to advances in sensitive optics and reconstruction methods [1]. Using time-resolved measurements, NLOS imaging recovers the 3D shape and appearance of objects outside the sensor’s line of sight, with applications in autonomous driving [2], 3D human pose estimation [3], and sensor systems [4], among others [5]–[7].

NLOS imaging can be categorized into two types: active [8]–[10] and passive [11], [12]. Passive NLOS imaging relies on ambient light, often resulting in high noise and low resolution. In contrast, active NLOS imaging uses photons from an active light source, capturing transient signals via time-of-flight (TOF) measurements [13], enabling effective spatiotemporal data collection. Common hardware setups include streak cameras with pulsed lasers, single-photon avalanche diodes (SPADs) [14] with pulsed lasers, and AMCW ToF cameras with modulated light sources, with SPADs and pulsed lasers being the most widely used. We focus on transient-based NLOS imaging, where hidden scene representation methods

are divided into two categories: volumetric albedo reconstruction [15]–[19] and object surface reconstruction [20]–[25]. Volumetric methods estimate albedo values of 3D voxels using techniques like filtered back-projection [15], [16], [26], light cone transform (LCT) [17], and phasor field (PF) [18]. Surface-based methods recover object surfaces by estimating surface normals, offering potential for detailed geometry capture [27]. However, current techniques face challenges such as limited applicability to complex scenes [20], sensitivity to noise [24] and initialization [22], and high computational costs [23].

For practical non-line-of-sight (NLOS) imaging, rapid data acquisition is essential. One approach is to improve the imaging system itself [8], [9], [28], while a more direct strategy involves reducing illumination points and shortening exposure times. However, this can result in incomplete data and higher noise levels, limiting the ability of direct methods to produce high-quality reconstructions. Iterative reconstruction methods leverage prior knowledge about transient measurements and objects to enhance image quality [29]–[36]. Techniques such as sparse priors, LASSO regularization [31], and total variation regularization [37] have been applied for target reconstruction. Additionally, collaborative regularization across multiple domains has been explored to restore low-quality transient signals and hidden details. For instance, methods like SOCR [32] and CNLOS [34], combined with volume-surface collaborative regularization (SSCR) [35], have been proposed. However, SOCR and SSCR rely on complex regularization techniques, while CNLOS introduces high-order gradient terms into the 3D volume. Both approaches significantly increase computational complexity, potentially offsetting the time savings from reduced data acquisition. Recent advances in deep learning have enabled neural networks to address NLOS imaging challenges [4], [38]–[43]. Yet, these methods heavily depend on training datasets. The lack of real-world NLOS imaging datasets remains a limitation, and mismatches between the distribution of real-world data and training data may significantly degrade reconstruction performance.

In this work, we propose a joint reconstruction model for volumetric albedo and surface details tailored for under-sampled transient data. As illustrated in Figure 1(b), our approach approximates volumetric albedo using two-dimensional depth and albedo maps. By applying effective regularization techniques to these maps, we significantly enhance the reconstruction quality of hidden scenes. Unlike LCT, which ignores normal information, and DLCT, which directly estimates normal albedo, we introduce a geometric prior for surface reconstruction to characterize the rate of change in surface normals, specifically by regularizing the shape operator to constrain the gradient field of the depth map (as shown in Figure 1(c)). Our method not only improves reconstruction quality by mitigating

X. Liu is with the Center for Applied Mathematics, Tianjin University, Tianjin 300072, China.

Y. Wang is with the School of Physics, Nankai University, China.

L. Wang, J. Liu and Y. Duan are with the School of Mathematical Sciences, Beijing Normal University, Beijing, 100875, China. E-mail: dove-duan@gmail.com

This paper was produced by the IEEE Publication Technology Group. They are in Piscataway, NJ.

Manuscript received April 19, 2021; revised August 16, 2021.

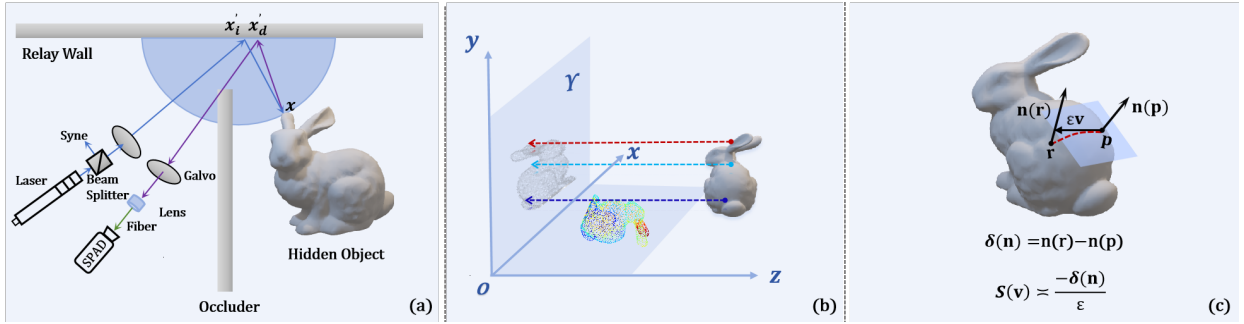


Fig. 1: Illustration of our geometric constrained non-line-of-sight imaging framework, where (a) NLOS system, (b) projection of volumetric albedo to albedo image (left side) and depth image (bottom), and (c) illustration of shape operator on surface.

blurring artifacts caused by the complexity of light propagation paths but also significantly reduces computational complexity by incorporating higher-order geometric constraints on the two-dimensional depth and albedo maps. To sum up, our main contributions are provided as follows

- We propose a joint reconstruction model for transient data, objects, and surfaces to address the challenges of under-sampled transient data under sparse illumination points and short exposure times.
- We introduce an effective geometric constraint for target surface reconstruction, enforcing sparsity in the gradient field of normals by minimizing the Frobenius norm of the shape operator, thereby ensuring surface continuity.
- We develop an efficient numerical algorithm that significantly reduces computational cost by implementing higher-order regularization and explicit computation strategies on two-dimensional depth and albedo functions.

## II. RELATED WORKS

Let  $\mathbf{x} = (x, y, z)$  be the three-dimensional scene coordinates, and  $\mathbf{x}'_i = (x'_i, y'_i, z = 0)$ ,  $\mathbf{x}'_d = (x'_d, y'_d, z = 0)$  be the illumination and detection coordinates on the visual wall, respectively. The laser sends a pulse of light towards point  $\mathbf{x}'_i$  on a visible wall, and the light diffusely scatters from that point. The scattered light illuminates the objects hidden around a corner, and a fraction of that light reflects back towards the wall in response. A transient sensor measures the temporal response at a point  $\mathbf{x}'_d$  on the wall. The transient measurement,  $\tau(\mathbf{x}'_i, \mathbf{x}'_d, t)$ , represents the amount of light detected at point  $\mathbf{x}'_d$  at time  $t$ . For simplicity, we omit the travel time between the system and the wall, which can be adjusted based on the wall's geometry relative to the laser and sensor positions. The image formation model is then given by

$$\tau(\mathbf{x}'_i, \mathbf{x}'_d, t) = \iiint_{\Omega} \frac{\langle \mathbf{x}'_i - \mathbf{x}, \mathbf{n}(\mathbf{x}) \rangle}{\|\mathbf{x}'_i - \mathbf{x}\|^3} \cdot \frac{\langle \mathbf{x}'_d - \mathbf{x}, \mathbf{n}(\mathbf{x}) \rangle}{\|\mathbf{x}'_d - \mathbf{x}\|^3} \cdot \delta(\|\mathbf{x} - \mathbf{x}'_i\| + \|\mathbf{x} - \mathbf{x}'_d\| - tc) u(\mathbf{x}) d\mathbf{x}. \quad (1)$$

The function  $u(\mathbf{x})$  represents the albedo of objects at each point  $\mathbf{x}$  within the 3D half-space  $\Omega$  where  $z > 0$ . Here,  $c$  denotes the speed of light, and  $\mathbf{n}(\mathbf{x}) = (n_x, n_y, n_z)(\mathbf{x})$  is the surface normal vector. The symbol  $\delta$  refers to the point-spread function (PSF). The expression inside the  $\delta$  relates the distance

light travels through the hidden volume to its time of flight. The denominator accounts for the decrease in the intensity of light as a function of distance traveled. When the illumination point and detection point are located at the same position, i.e.,  $\mathbf{x}' = \mathbf{x}'_i = \mathbf{x}'_d$ , the model (1) reduces to

$$\tau(\mathbf{x}', t) = \iiint_{\Omega} \frac{\langle \mathbf{x}' - \mathbf{x}, \mathbf{n}(\mathbf{x}) \rangle}{\|\mathbf{x}' - \mathbf{x}\|^3} \cdot \frac{\langle \mathbf{x}' - \mathbf{x}, \mathbf{n}(\mathbf{x}) \rangle}{\|\mathbf{x}' - \mathbf{x}\|^3} \cdot \delta(2\|\mathbf{x} - \mathbf{x}'\| - tc) u(\mathbf{x}) d\mathbf{x}.$$

### A. The Light-cone transform (LCT)

In [17], by assuming that light scattering on the object surface is isotropic, it can further simplify the geometry of light propagation as follows

$$\tau(\mathbf{x}', t) = \iiint_{\Omega} \frac{u(\mathbf{x})}{\|\mathbf{x}' - \mathbf{x}\|^4} \delta(2\|\mathbf{x}' - \mathbf{x}\| - tc) d\mathbf{x}, \quad (2)$$

the discrete problem of which gives

$$\tau = Au \quad (3)$$

with  $A$  being the light transport matrix. The inverse problem (3) can be efficiently solved via Wiener filtering in the Fourier domain, known as the light-cone transform (LCT). While LCT effectively reconstructs the shapes of hidden objects, as a low-pass filter, it fails to accurately model the light reflection behavior of surface materials with anisotropic scattering properties.

### B. The Directional Light-cone transform (DLCT)

Young et al. [24] introduced the directional-albedo variable, i.e.,  $\mathbf{v}(v_x, v_y, v_z)(\mathbf{x}) = u(\mathbf{x})\mathbf{n}(\mathbf{x})$ , allowing to obtain the complex surface details. Thus, the forward model (1) becomes

$$\tau(\mathbf{x}', t) = \iiint_{\Omega} \frac{\langle \mathbf{v}(\mathbf{x}), \mathbf{x}' - \mathbf{x} \rangle}{\|\mathbf{x}' - \mathbf{x}\|^5} \cdot \delta(2\|\mathbf{x} - \mathbf{x}'\| - tc) d\mathbf{x}.$$

The corresponding inverse problem is a vectorial form of the model (3) and can be efficiently solved using Cholesky-Wiener decomposition. The directional LCT model simulates light reflection and propagation on surfaces with complex geometries and materials. While effective at detailing fine surface structures, it struggles to represent an object's overall shape and potentially overlook large-scale features or complex

forms due to amplified noise. Additionally, since the light transport matrix  $A$  acts as a low-pass filter with a high condition number, both LCT and DLCT reconstructions can degrade significantly in the presence of data loss or noise.

### III. OUR METHOD

#### A. Sparse NLOS

NLOS imaging can be accelerated using transient data with short exposure times and sparse illumination points, which can be mathematically formulated as follows

$$\tau_0 = SAu + \epsilon, \quad (4)$$

where  $\epsilon$  is random noise,  $S$  is the selection matrix, and  $\tau_0$  is transient data acquired using sparse illumination points. We aim to solve the inverse problem (4) to estimate the hidden object  $u$  from  $\tau_0$ . Using Bayesian estimation, we combine observed data with prior knowledge to obtain the solution. Specifically, we integrate the data with the prior distribution to derive the posterior distribution, addressing uncertainty and noise in the data. The joint probability of observing both  $u$  and  $\tau_0$  is given as follows

$$P(u|\tau_0) = \frac{P(\tau_0|u)P(u)}{P(\tau_0)},$$

where  $P(u|\tau_0)$  is the posterior probability,  $P(\tau_0|u)$  is the likelihood function,  $P(u)$  is the prior probability and  $P(\tau_0)$  is the marginal likelihood. By introducing  $\tau$ , we can reformulate it as

$$P(u, \tau|\tau_0) = \frac{P(\tau_0|u, \tau)P(\tau|u)P(u)}{P(\tau_0)}.$$

We assume that  $u$  depends solely on the reconstructed transient data, i.e.,  $P(\tau_0|u, \tau) = P(\tau_0|\tau)$ . Based on Bayes' theorem and the Maximum a Posteriori (MAP) estimator, maximizing the posterior probability of  $u$  and  $\tau$  given  $\tau_0$  is equivalent to minimizing the negative log-likelihood

$$(u^*, \tau^*) = \arg \min_{u, \tau} -\log P(\tau_0|\tau) - \log P(\tau|u) - \log P(u). \quad (5)$$

Assuming the noise in the transient data is additive Gaussian noise and incorporating the sparsity prior of the 3D object, we derive the minimization problem from (5) as

$$E_1(u, \tau) = \frac{1}{2} \int_{\Omega} (Au - \tau)^2 + \frac{\rho}{2} \int_{\Omega} (S\tau - \tau_0)^2 + \gamma \int_{\Omega} |u| dx, \quad (6)$$

where  $\rho$  governs the consistency between the updated and initial signals, and  $\gamma$  adjusts the weight of the sparsity term, defined as

$$\gamma = \sigma * \sum_{x, y, t} \tau_0(x, y, t)$$

with  $\sigma$  being a tunable positive parameter. Here,  $\gamma$  is used to model the dependency relationship between  $u$  and  $\tau_0$ .

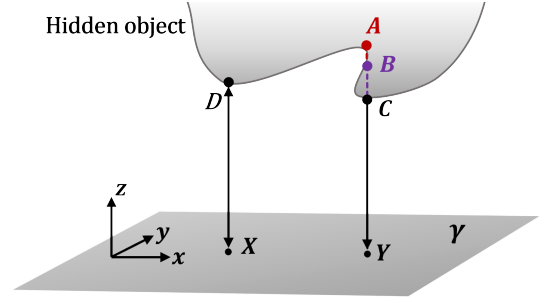


Fig. 2: The projection operator between volumetric albedo and 2D albedo map.

#### B. Geometric constrained surface reconstruction

Object reconstruction aims to align with the NLOS target surface where photons land. We project the surface onto a two-dimensional plane and utilize the depth map of the surface to represent the object's surface. As Fig. 1 (b), let  $\Upsilon := (x, y, z = 0) \in \Omega$  define the projection plane of the hidden object. The position of each point is determined by its distance to the projection plane. For a given position  $(x, y) \in \Upsilon$ , let  $n_{xy}$  denote the number of nonzero  $u(x, y, \cdot)$  values along the depth direction. If  $n_{xy}$  is nonzero, the corresponding depth values are represented by  $z_i$  for  $i = 1, \dots, n_{xy}$ , ordered from smallest to largest. A depth image  $D$  and an albedo image  $I$  can be derived from  $u$  using the weighted projection function  $(I, D) := P(u)$ , defined as

$$\begin{cases} I_{xy} := (P_I(u))_{xy} = \chi(n_{xy}) \cdot \sum_{i=1}^{n_{xy}} \omega_{xyz_i} \cdot u_{xyz_i}, \\ D_{xy} := (P_D(u))_{xy} = \left[ \chi(n_{xy}) \cdot \sum_{i=1}^{n_{xy}} \omega_{xyz_i} \cdot z_i \right], \end{cases}$$

where  $\chi(\cdot)$  is the indicator function is  $\chi(x) = 1$  for  $x \neq 0$  and  $\chi(x) = 0$  for  $x = 0$ , and  $[\cdot]$  is the rounding operation. The weights are estimated using

$$\omega_{xyz_i} = u_{xyz_i}^p / \sum_{j=1}^{n_{xy}} u_{xyz_j}^p, \quad (7)$$

where  $p$  denotes the power of  $u$ . It indicates that higher albedo contributes greater weight.

As shown in Fig. 2, a non-reversible many-to-one mapping is established, particularly for non-convex surfaces. However, the hidden object  $u$  can be approximated using a depth image  $D$  and an albedo image  $I$  via back-projection

$$u_{xyD_{xy}} := P^\dagger(I, D) = \begin{cases} I_{xy}, & \text{for } D_{xy} \neq 0, \\ 0, & \text{for } D_{xy} = 0, \end{cases}$$

where  $P^\dagger(\cdot, \cdot)$  is the selective inverse function used to reconstruct the hidden object. Let  $\mathbb{S} = (x, y, D(x, y))$  be the surface defined in  $(x, y) \in \Upsilon$ , which corresponds to the zero level set of  $\phi(x, y, z) = z - D(x, y)$ . Since surface normals are crucial for accurately estimating and recovering the shape of the surface, we first define the *unit normal* of the zero level set  $\{(x, y, z) : \phi(x, y, z) = 0\}$  as [44]

$$N_D = \frac{\nabla \phi}{|\nabla \phi|} = \frac{(\nabla D, -1)}{\sqrt{1 + |\nabla D|^2}},$$

---

**Algorithm 1** The ADMM-based algorithm for the joint reconstruction model

---

**Input:** Raw data  $\tau_0$ , and parameters  $\gamma, \rho, \eta, \lambda, I^0 = 0, D^0 = 0, K_{max}$ ;  
*/\* Initialize the variable  $u$  \*/*  
 $u^0 = \arg \min_u \frac{1}{2} \int_{\Omega} (A_S u - \tau_0)^2 dx + \gamma \int_{\Omega} |u| dx$ ;  
**for**  $k = 0$  **to**  $K_{max} - 1$  **do**  
*/\* Compute  $\tau^{k+1}$  \*/*  
 $\tau^{k+1} = \arg \min_{\tau} \frac{1}{2} \int_{\Omega} (A u^k - \tau)^2 dx + \frac{\rho}{2} \int_{\Omega} (S \tau - \tau_0)^2 dx$ ;  
*/\* Compute  $D^{k+1}$  \*/*  
 $D^{k+1} = \arg \min_D \frac{1}{2} \int_{\Upsilon} (D - P_D(u^k))^2 dx + \int_{\Upsilon} |\alpha(D^k)| |\nabla D| dx + \int_{\Upsilon} \beta(D^k) |\nabla^2 D|_F dx$ ;  
*/\* Compute  $I^{k+1}$  \*/*  
 $I^{k+1} = \arg \min_I \frac{1}{2} \int_{\Upsilon} (I - P_I(u^k))^2 dx + \eta \int_{\Upsilon} |\nabla I| dx$ ;  
*/\* Compute  $u^{k+1}$  \*/*  
 $u^{k+1} = \arg \min_u \frac{1}{2} \int_{\Omega} (A u - \tau^{k+1})^2 dx + \frac{\lambda}{2} \int_{\Omega} (u - P^{\dagger}(I^{k+1}, D^{k+1}))^2 dx + \gamma \int_{\Omega} |u| dx$ ;  
**end for**  
**Output:**  $u^{K_{max}}$ .

---

where  $\nabla D$  is the gradient of  $D$ . Surface normal smoothness is a key prior to reduce noise and unnatural discontinuities. We use the shape operator as a regularization for the depth map, as it captures the surface geometry, including curvature and bending. It provides a linear map that relates changes in the normal vector along the surface. Specifically, the shape operator is defined as:

$$\begin{aligned} \mathcal{S}(D) &= \nabla \left( \frac{\nabla D}{\sqrt{1 + |\nabla D|^2}} \right) \\ &= \nabla \frac{1}{\sqrt{1 + |\nabla D|^2}} \otimes \nabla D + \frac{1}{\sqrt{1 + |\nabla D|^2}} \nabla^2 D, \end{aligned}$$

where  $\nabla^2 D$  is the Hessian of  $D$  and  $\otimes$  is the Euclidean outer product. Regularizing the sparsity of the shape operator helps balance smoothness and geometric detail, reducing deformations caused by excessive bending or noise [45]. Thus, we apply a shape operator sparsity prior to the depth map yielding  $P(D) \propto \exp(-S(D))$ . Additionally, we assume the albedo map  $I$  follows a total variation (TV) prior to preserve edges and reduce noise. Consequently, we formulate the following energy functional to recover both the albedo and depth maps

$$\begin{aligned} E_2(u, D, I) &= \lambda \mathcal{M}(u, P^{\dagger}(I, D)) + \eta \int_{\Upsilon} |\nabla I| dx \\ &\quad + \int_{\Upsilon} |\alpha(D) \otimes \nabla D + \beta(D) \nabla^2 D|_F dx, \end{aligned}$$

where  $\lambda$  and  $\eta$  are positive parameters,  $\mathcal{M}(u, P^{\dagger}(I, D))$  is used to measure the distance between the hidden object and the back-projection surface in terms of the  $L_2$  norm, and  $|\cdot|_F$  is the Frobenius norm. Besides, we denote

$$\alpha(D) = \nabla \frac{1}{\sqrt{1 + |\nabla D|^2}}, \quad \beta(D) = \frac{1}{\sqrt{1 + |\nabla D|^2}}.$$

*C. Geometric constrained NLOS reconstruction*

To address sparse illumination and low-exposure NLOS reconstruction, we jointly reconstruct the hidden object and measured surface, deriving the following model

$$\min_{u, \tau, D, I} E(u, \tau, D, I) := E_1(u, \tau) + E_2(u, D, I), \quad (8)$$

which allows for higher-quality reconstruction by incorporating geometric surface constraints.

IV. SOLUTIONS AND ALGORITHM

We now present the numerical minimization approach for the proposed model (8), where the four variables are iteratively and alternatively solved as outlined in Algorithm 1. In our algorithm, the variable  $u$  is initialized by solving the following minimization problem

$$\min_u \frac{1}{2} \int_{\Omega} (A_S u - \tau_0)^2 dx + \gamma \int_{\Omega} |u| dx, \quad (9)$$

where  $A_S = SA$ . This problem is solved using the Fast Iterative Shrinkage-Thresholding Algorithm (FISTA). Below, we will discuss the solution to each subproblem in detail.

*A. Sub-minimization problem w.r.t. the variable  $\tau$*

The sub-minimization problem w.r.t.  $\tau$  can be expressed as

$$\min_{\tau} \frac{1}{2} \int_{\Omega} (A u - \tau)^2 dx + \frac{\rho}{2} \int_{\Omega} (S \tau - \tau_0)^2 dx,$$

which is a quadratic minimization problem. The close-form solution is given as follows

$$\tau^{k+1} = \begin{cases} A u^k, & \text{for } S(x, y, t) = 0, \\ (A u^k + \rho \tau_0) / (\rho + 1), & \text{for } S(x, y, t) = 1, \end{cases}$$

and  $\tau_0$  is the sparse transient data.

*B. Sub-minimization problem w.r.t. the variable  $D$*

According to  $E_2$ , the sub-minimization problem w.r.t the variable  $D$  is defined as

$$\min_D \frac{1}{2} \int_{\Upsilon} (D - P_D(u))^2 + \int_{\Upsilon} |\alpha(D) \otimes \nabla D + \beta(D) \nabla^2 D|_F dx.$$

If we explicitly update  $\alpha(D)$  and  $\beta(D)$  as the weights for the first- and second-order gradient operators, the computational complexity can be effectively reduced, transforming the original problem into

$$\min_D \frac{1}{2} \int_{\Upsilon} (D - P_D(u))^2 dx + \int_{\Upsilon} |\alpha(D)| |\nabla D| dx + \int_{\Upsilon} \beta(D) |\nabla^2 D|_F dx. \quad (10)$$

By introducing auxiliary variable  $v = \nabla D$  and  $w = \nabla^2 D$ , we can rewrite (10) into a constrained minimization problem

$$\min_{D,v,w} \frac{1}{2} \int_{\Upsilon} (D - P_D(u))^2 + \int_{\Upsilon} \alpha(x)|v| + \int_{\Upsilon} \beta(x)|w|_F dx$$

s.t.  $v = \nabla D, w = \nabla^2 D.$

Its augmented Lagrangian functional is defined as follows

$$\begin{aligned} \mathcal{L}(D, v, w; \Lambda_1, \Lambda_2) = & \frac{1}{2} \int_{\Upsilon} (D - P_D(u))^2 + \int_{\Upsilon} \alpha(x)|v| dx \\ & - \int_{\Upsilon} \Lambda_1 (v - \nabla D) + \frac{r_1}{2} \int_{\Upsilon} (v - \nabla D)^2 + \int_{\Upsilon} \beta(x)|w|_F dx \\ & - \int_{\Upsilon} \Lambda_2 (w - \nabla^2 D) + \frac{r_2}{2} \int_{\Upsilon} (w - \nabla^2 D)^2 dx, \end{aligned} \quad (11)$$

where  $\Lambda_1$  and  $\Lambda_2$  are Lagrange multipliers, and  $r_1, r_2$  are the positive penalty parameters. One immediately gets the saddle-point problem below

$$\max_{\Lambda_1, \Lambda_2} \min_{v, w, D} \mathcal{L}(v, w, D; \Lambda_1, \Lambda_2),$$

which is further handled by alternative minimization w.r.t. the variables  $v, w$  and  $D$ , respectively.

1) *Sub-minimization problem w.r.t. the variable  $v$* : The sub-minimization problem w.r.t. the variable  $v$  is defined as

$$\min_v \int_{\Upsilon} \alpha(x)|v| dx + \frac{r_1}{2} \int_{\Upsilon} \left( v - \nabla D - \frac{\Lambda_1}{r_1} \right)^2 dx,$$

where  $v^{k+1}$  can be computed through the shrinkage operator as follows

$$v^{k+1} = \text{shrinkage} \left( \nabla D^k + \frac{\Lambda_1^k}{r_1}, \frac{\alpha(D^k)}{r_1} \right)$$

with  $\text{shrinkage}(a, \xi) = \max\{|a| - \xi, 0\} \frac{a}{|a|}$ , for  $a \in \mathbb{R}^n$ .

2) *Sub-minimization problem w.r.t. the variable  $w$* : The sub-minimization problem w.r.t. the variable  $w$  is defined as follows

$$\min_w \int_{\Upsilon} \beta|w|_F dx + \frac{r_2}{2} \int_{\Upsilon} \left( w - \nabla^2 D - \frac{\Lambda_2}{r_2} \right)^2 dx,$$

where  $w^{k+1}$  can also be computed by the shrinkage operator

$$w^{k+1} = \text{shrinkage}_F \left( \nabla^2 D^k + \frac{\Lambda_2^k}{r_2}, \frac{\beta(D^k)}{r_2} \right)$$

with the shrinkage operator defined in terms of the Frobenius norm.

3) *Sub-minimization problem w.r.t. the variable  $D$* : The sub-minimization problem w.r.t. the variable  $D$  is defined as

$$\min_D \frac{1}{2} \int_{\Upsilon} \left( D - P_D(u) \right)^2 + \frac{r_1}{2} \int_{\Upsilon} \left( \nabla D - \left( v - \frac{\Lambda_1}{r_1} \right) \right)^2 dx + \frac{r_2}{2} \int_{\Upsilon} \left( \nabla^2 D - \left( w - \frac{\Lambda_2}{r_2} \right) \right)^2 dx.$$

Given the variables  $v^{k+1}, \omega^{k+1}, \Lambda_1^k, \Lambda_2^k$ , the Euler-Lagrange equation of the above subproblem can be obtained by

$$\begin{aligned} D - P_D(u^k) - r_1 \text{div} \left( \nabla D - \left( v^{k+1} - \frac{\Lambda_1^k}{r_1} \right) \right) \\ + r_2 \text{div}^2 \left( \nabla^2 D - \left( w^{k+1} - \frac{\Lambda_2^k}{r_2} \right) \right) = 0. \end{aligned}$$

We can solve the above PDE by Fast Fourier Transform (FFT), which gives

$$D^{k+1} = \mathcal{F}^{-1} \left( \frac{\mathcal{F}(P_D(u^k) - \text{div}(r_1 v^{k+1} - \Lambda_1^k) + \text{div}^2(r_2 w^{k+1} - \Lambda_2^k))}{(\mathcal{I} - r_1 \mathcal{F} \Delta \mathcal{F}^{-1} + r_2 \mathcal{F} \Delta^2 \mathcal{F}^{-1})} \right),$$

where  $\mathcal{F}$  and  $\mathcal{F}^{-1}$  represent the forward and inverse FFT, respectively.

4) *Update of  $\alpha$  and  $\beta$* : Both  $\alpha$  and  $\beta$  are adaptively updated according to the following rules

$$\begin{cases} \alpha(D^{k+1}) = \nabla \frac{1}{\sqrt{1 + |\nabla D^{k+1}|^2}}, \\ \beta(D^{k+1}) = \frac{1}{\sqrt{1 + |\nabla D^{k+1}|^2}}. \end{cases}$$

5) *Update of Lagrange multipliers*: The initial values of the Lagrange multipliers  $\Lambda_1$  and  $\Lambda_2$  are set to zero. They are updated through a standard dual-ascent rule from:

$$\begin{cases} \Lambda_1^{k+1} = \Lambda_1^k + r_1 (\nabla D^{k+1} - v^{k+1}), \\ \Lambda_2^{k+1} = \Lambda_2^k + r_2 (\nabla^2 D^{k+1} - w^{k+1}). \end{cases}$$

C. *Sub-minimization problem w.r.t.  $I$*

The minimization problem w.r.t. the albedo function  $I$  is given as follows

$$\min_I \frac{1}{2} \int_{\Upsilon} (I - P_I(u))^2 dx + \int_{\Upsilon} \eta |\nabla I| dx,$$

which is a typical total variation minimization problem. By introducing an auxiliary variable  $q = \nabla I$ , we can rewrite the above equation into a constrained minimization problem as

$$\min_{I,q} \frac{1}{2} \int_{\Upsilon} (I - P_I(u))^2 dx + \int_{\Upsilon} \eta |q| dx$$

s.t.  $q = \nabla I,$

and the corresponding augmented Lagrangian is as follows

$$\begin{aligned} \mathcal{L}(I, q; \Lambda_3) = & \frac{1}{2} \int_{\Upsilon} (I - P_D(u))^2 dx + \int_{\Upsilon} \eta |q| dx \\ & - \int_{\Upsilon} \Lambda_3 (q - \nabla I) dx + \frac{r_3}{2} \int_{\Upsilon} (q - \nabla I)^2 dx. \end{aligned}$$

Similarly, the saddle point problem is formulated as

$$\max_{\Lambda_3} \min_{q, I} \mathcal{L}(q, I; \Lambda_3),$$

which can be further split into two sub-minimization problems w.r.t.  $q$  and  $I$ , respectively.

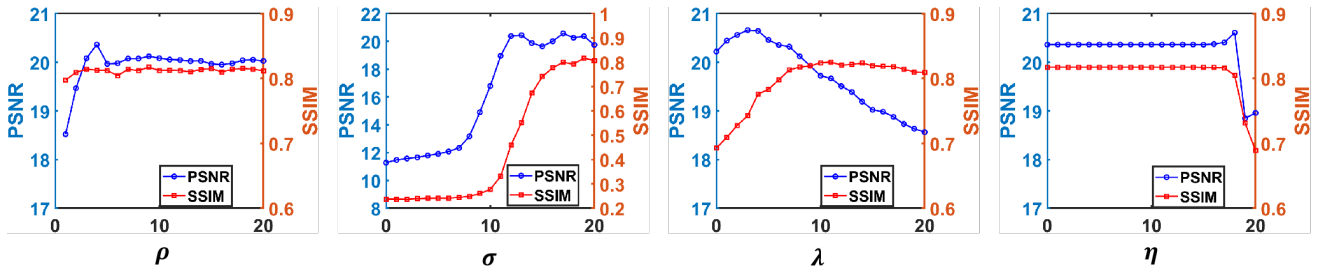


Fig. 3: Performance of our SLCT model in terms of both SSIM and PSNR with different model parameters  $\rho$ ,  $\sigma$ ,  $\lambda$ , and  $\eta$ .

1) *Sub-minimization problem w.r.t. the variable  $q$* : The sub-minimization problem w.r.t.  $q$  is defined as

$$\min_q \int_{\Upsilon} \eta |q| dx + \frac{r_3}{2} \int_{\Upsilon} \left( q - \nabla I - \frac{\Lambda_3}{r_3} \right)^2 dx,$$

which can be solved through the soft thresholding operator

$$q^{k+1} = \text{shrinkage} \left( \nabla I^k + \frac{\Lambda_3^k}{r_3}, \frac{\eta}{r_3} \right).$$

2) *Sub-minimization problem w.r.t. the variable  $I$* : The sub-minimization problem w.r.t.  $I$  is defined as

$$\min_I \frac{1}{2} \int_{\Upsilon} (I - P_I(u))^2 dx + \frac{r_3}{2} \int_{\Upsilon} \left( \nabla I - \left( q - \frac{\Lambda_3}{r_3} \right) \right)^2 dx.$$

Given the fixed variables  $q^{k+1}$  and  $\Lambda_3^k$ , the relevant Euler-Lagrange equation is defined as

$$I - P_I(u^k) - r_3 \text{div} \left( \nabla I - \left( q^{k+1} - \frac{\Lambda_3^k}{r_3} \right) \right) = 0,$$

which can be solved by FFT as follows

$$I^{k+1} = \mathcal{F}^{-1} \left( \frac{\mathcal{F}(P_I(u^k) - \text{div}(r_3 q^{k+1} - \Lambda_3^k))}{\mathcal{I} - r_3 \mathcal{F} \Delta \mathcal{F}^{-1}} \right).$$

3) *Update of Lagrange multipliers*: The initial value  $\Lambda_3^0 = 0$  and it can be updated from

$$\Lambda_3^{k+1} = \Lambda_3^k + r_3 (\nabla I^{k+1} - q^{k+1}).$$

D. *Sub-minimization problem w.r.t.  $u$*

Since both energy functional  $E_1$  and  $E_2$  contain the variable  $u$ , the sub-minimization problem w.r.t.  $u$  can be given as

$$\min_u \frac{1}{2} \int_{\Omega} (Au - \tau)^2 + \frac{\lambda}{2} \int_{\Omega} (u - P^\dagger(I, D))^2 + \gamma \int_{\Omega} |u| dx,$$

which can be solved by the Fast Iterative Shrinkage-Thresholding Algorithm (FISTA) [46]. Thus,  $u^{k+1}$  is updated by

$$u^{k+1} = \text{shrinkage} \left( \bar{u}^k - t[A^T(A\bar{u}^k - \tau^{k+1}) + \lambda(\bar{u}^k - P^\dagger(I^{k+1}, D^{k+1}))], \gamma t \right),$$

where  $\bar{u}$  is an extrapolation variable used to accelerate updates. Initially,  $\bar{u}^0 = u^0$  and  $\mu^0 = 1$ . The extrapolation variable is updated iteratively using

$$\begin{cases} \bar{u}^{k+1} = u^{k+1} + \frac{\mu^k - 1}{\mu^{k+1}} (u^{k+1} - u^k), \\ \mu^{k+1} = (1 + \sqrt{1 + 4(\mu^k)^2})/2. \end{cases}$$

The iterative step size  $t$  is chosen to balance the algorithm's convergence and convergence speed. A suitable choice for  $t$  is  $1/(||A||_2^2 + \lambda)$ .

## V. EXPERIMENTAL RESULTS

All our experiments are conducted on a workstation equipped with an Intel Xeon Gold 6132 CPU and an NVIDIA TITAN RTX GPU. Both the CNLOS method and our approach are GPU-accelerated and implemented on the same GPU. To illustrate the effectiveness of our proposed method in improving both the quality and efficiency of NLOS imaging reconstruction. We compare it with existing methods (i.e., LCT [17], DLCT [24], PF [18], SPIRAL [31], SSCR [35], CNLOS [34]). Experimental validation is implemented on the Zaragoza [47], Stanford [19], USTC [39] and NLoS benchmark [48] datasets.

### A. Data description and preprocessing

The datasets 'usaf', 'serapis', and 'bunny' are from the Zaragoza dataset, with original dimensions of 256×256, 256×256, and 64×64, and wall sizes of 1m×1m, 1m×1m, and 0.6m×0.6m, respectively. Each scenario has 512 time bins, with photons traveling 0.003m, 0.003m, and 0.0025m per bin. We preprocess the data by uniformly sampling and resizing it to 64×64×512. The datasets 'statue', 'dragon', 'outdoor', and 'teaser' are from the Stanford dataset. The raw measurement size for 'outdoor' is 128×128×2048, while the others are 512×512×2048, all with a wall size of 2m×2m. The time resolution is cropped to 512 bins, each spanning 32 ps. 'Statue', 'dragon', and 'outdoor' are uniformly sampled and resized to 64×64. According to [39], 'teaser' is preprocessed to 256×256 and further reduced to 128×128 by aggregating every 2×2 points. The 'man letter' dataset is from the USTC dataset, with dimensions of 128×128×512, a wall size of 2m×2m, and each time bin spanning 32 ps. The non-confocal data 'k' is from the NLOS benchmark dataset, with a wall size of 0.256m×0.256m and photons traveling 0.001m per bin. For our experiments, we use data downsampled to 64×64, as provided by [32]. It includes 1024 time bins.

### B. Parameter discussing

Our model includes six parameters:  $\rho$ ,  $\sigma$ ,  $\lambda$ ,  $\eta$ ,  $\alpha$ , and  $\beta$ , where  $\alpha$  and  $\beta$  are adaptively updated based on depth values. The algorithm also incorporates penalty parameters  $r_1$ ,  $r_2$ , and  $r_3$ , with appropriate values accelerating convergence. Since most experiments are performed on undersampled measurements, we evaluate the impact of these parameters on the dragon scene at a 16×16 scanning points.



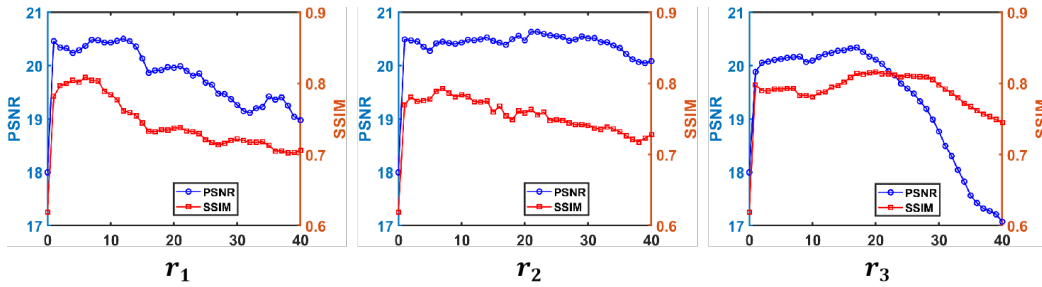


Fig. 4: Performance of our SLCT model in terms of both SSIM and PSNR with different algorithm parameters  $r_1$ ,  $r_2$ , and  $r_3$ .

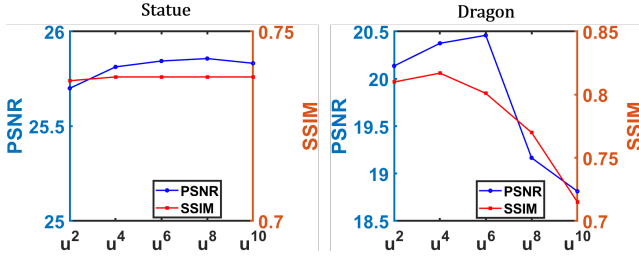


Fig. 5: Evaluation of model performance with different powers of  $u$ .

Fig. 3 illustrates the impact of varying model parameters on the results. The ranges for  $\rho$ ,  $\sigma$ , and  $\lambda$  are  $[0, 100]$ ,  $[0, 1e-5]$ , and  $[0, 1]$ , respectively, with 20 uniformly selected values tested for each. For  $\eta$ , ranging from  $[0, 1e-1]$ , 20 logarithmically spaced values are tested. The results indicate that our model is less sensitive to  $\rho$  and  $\eta$  within certain ranges, which can be fixed as  $\rho = 25$  and  $\eta = 1e - 5$ . However, our model is sensitive to  $\sigma$  and  $\lambda$ , necessitating careful case-by-case tuning. The algorithm parameters  $r_1$ ,  $r_2$ , and  $r_3$  have ranges of  $[0, 0.8]$ ,  $[0, 8]$ , and  $[0, 40]$ , respectively, with 40 uniformly selected values tested. As shown in Fig. 4, all algorithm parameters can also be fixed, specifically  $r_1 = 0.1$ ,  $r_2 = 2$ , and  $r_3 = 20$ . Additionally, we investigate the impact of the power  $p$  in the weight calculation (7). While a higher power emphasizes larger  $u$  values, it does not always improve results. As shown in Fig. 5, in the dragon scenario, high weights may amplify noise, resulting in a significant decrease in the SSIM value. Thus, we fix the power  $p = 4$ .

We also discuss the algorithm’s iteration count in two different scenarios. As shown in Fig. 6, with an increase in iterations, the relative error decreases and the metric values stabilize. We consider both the time cost and the quality of the image reconstruction and set the maximum number of iterations to 120.

### C. Comparison among LCT, DLCT and our SLCT

We conduct a qualitative comparison of LCT and DLCT on the Zaragoza dataset. As shown in Fig. 7, our SLCT method achieves high-quality reconstruction across all scenes. With sufficient illumination points, SLCT provides more accurate reconstruction results in the first two scenes and performs comparably to DLCT in the serapis scene. However, as the number of illumination points decreases, the performance of LCT and DLCT significantly degrades, particularly in the detail-rich

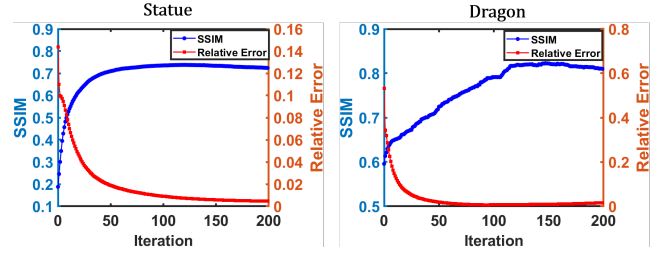


Fig. 6: Relative error  $|u^{k+1} - u^k| / |u^k|$  and SSIM w.r.t. different numbers of iterations.

serapis scene, where DLCT generates severe background noise that cannot be effectively removed through post-processing. This indicates that the normal vector estimation errors in DLCT increase significantly with fewer illumination points and higher noise levels, leading to a decline in reconstruction quality. In contrast, our method consistently reconstructs superior shapes and details under sparse illumination conditions, demonstrating stronger robustness.

Additionally, we investigate the impact of post-processing on non-line-of-sight imaging results. Three common post-processing techniques are employed across different methods to enhance reconstruction quality: truncation removes outliers, thresholding eliminates smaller values, and Gaussian smoothing refines the image. Fig. 8 demonstrates the effects of these techniques on the reconstruction of the serapis scene under full sampling conditions. Evidently, compared to our method, direct approaches such as LCT and DLCT exhibit a stronger dependence on post-processing. In subsequent experiments, we apply appropriate post-processing to the results of different methods. As individually adjusting post-processing for each image is time-consuming and inefficient for non-line-of-sight imaging, in later real-data experiments, we use a consistent post-processing approach for the same method across different scanning points within the same scene.

### D. Comparison results on real measurement data

We present reconstruction results for the ‘statue’ scene using various methods. As shown in Fig. 9, direct methods such as DLCT and PF produce high-quality results with a higher number of scanning points. However, as the number of illumination points decreases, these methods show increased background noise compared to iterative approaches, with all methods experiencing performance degradation. In contrast, our SLCT method captures more details even with only

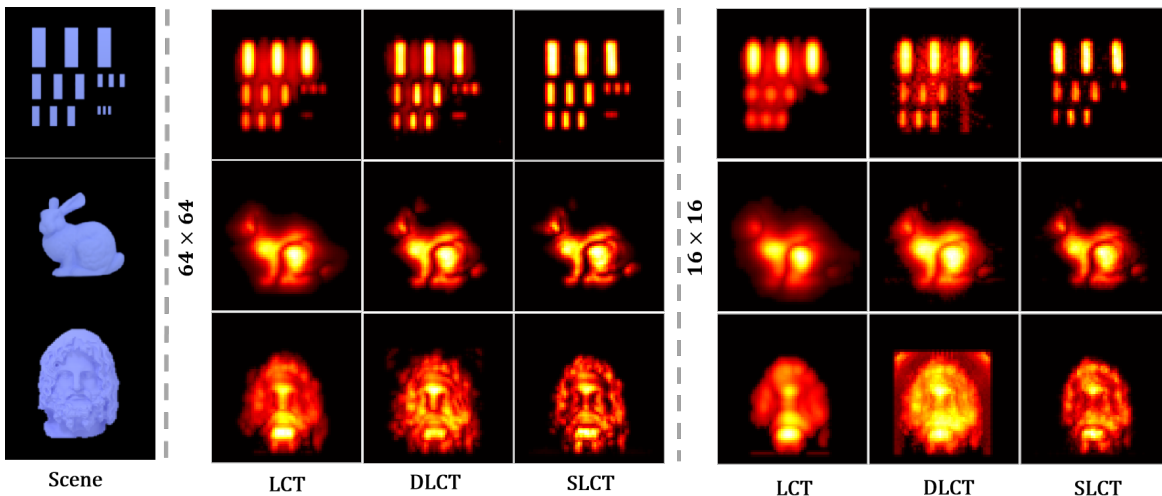


Fig. 7: Comparison results on ‘usaf’, ‘bunny’ and ‘serapis’ with  $64 \times 64$  and  $16 \times 16$  scanning points. The parameters of our methods are set as:  $\sigma = 5e - 7$ ,  $\lambda = 0.02$  (usaf),  $\sigma = 5e - 7$ ,  $\lambda = 0.02$  (bunny),  $\sigma = 5e - 7$ ,  $\lambda = 0.02$  (serapis) for  $64 \times 64$  scanning points;  $\sigma = 8e - 6$ ,  $\lambda = 0.02$  (usaf),  $\sigma = 1e - 6$ ,  $\lambda = 0.04$  (bunny),  $\sigma = 4e - 6$ ,  $\lambda = 0.03$  (serapis) for  $16 \times 16$  scanning points.

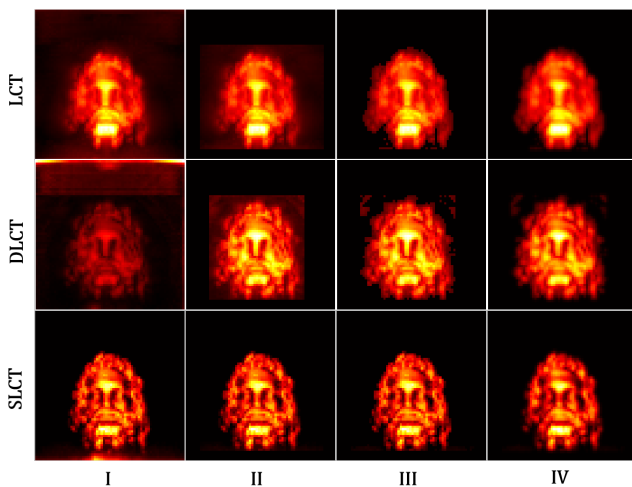


Fig. 8: The impact of post-processing methods on the results. I: No post-processing; II: Truncation post-processing; III: Truncation and thresholding post-processing; IV: Truncation, thresholding and Gaussian smoothing post-processing.

$12 \times 12$  scanning points. Table I provides evaluation metrics, demonstrating that SLCT consistently achieves higher PSNR and SSIM values across all scenes. Our SLCT achieves higher reconstruction accuracy with only  $16 \times 16$  scanning points than direct methods at  $28 \times 28$  scanning points, while requiring less total time than the fastest direct method. This highlights the importance of reducing scanning points to accelerate NLOS reconstruction.

We compared various methods on the ‘dragon’ scene under different exposure times and scanning points. The dragon’s metallic surface introduces more light scattering noise than the ‘statue’ scene, increasing background noise for direct methods. SPIRAL, an iterative method, produces rough reconstructions but is highly noise-sensitive. SSCR also suffers from noise, leading to significant albedo loss. While CNLOS excels on

smooth surfaces, its strong continuity priors for 3D curvature and volumetric reflectance result in fine detail loss. In contrast, SLCT achieves the highest reconstruction resolution. Table II provides quantitative metrics, validating the robustness of our approach. Our method achieves comparable accuracy while significantly reducing processing time, offering over  $30 \times$  speedup compared to SSCR and reducing reconstruction time to one-third of GPU-accelerated CNLOS.

We compared our method with other established approaches in complex scenes. As shown in Fig. 11, LCT and PF are limited to reconstructing only the outlines of hidden objects. DLCT captures subtle details by incorporating normal vectors, but this results in significant noise. Iterative methods, however, reveal the fine structure of objects and identify specific features. Specifically, CSA introduces noticeable background noise and albedo loss, while CNLOS produces overly smooth reconstructions, particularly at the boundaries. Our SLCT method effectively reduces noise and better preserves texture, achieving the highest resolution. Additionally, our method offers the fastest reconstruction time among iterative methods.

### E. Ablation studies

In Table III, we conduct ablation studies using real measurement data from the Stanford dataset to validate the effectiveness of our model. Setup I serves as the baseline, incorporating only  $L_1$  regularization on the reconstructed image. Setup II enhances this by adding a transient data inpainting module, improving PSNR by 0.5 dB and 0.4 dB in two scenarios, albeit at the cost of reduced SSIM. Setup III, our proposed SLCT model, introduces geometric constraints, significantly improving both reconstruction accuracy and resolution, with notable gains in PSNR and SSIM. Fig. 13 demonstrates that SLCT achieves the most accurate shape reconstructions, particularly in the head and body of the person in the outdoor scene, as well as the dragon’s body. Both qualitative and quantitative



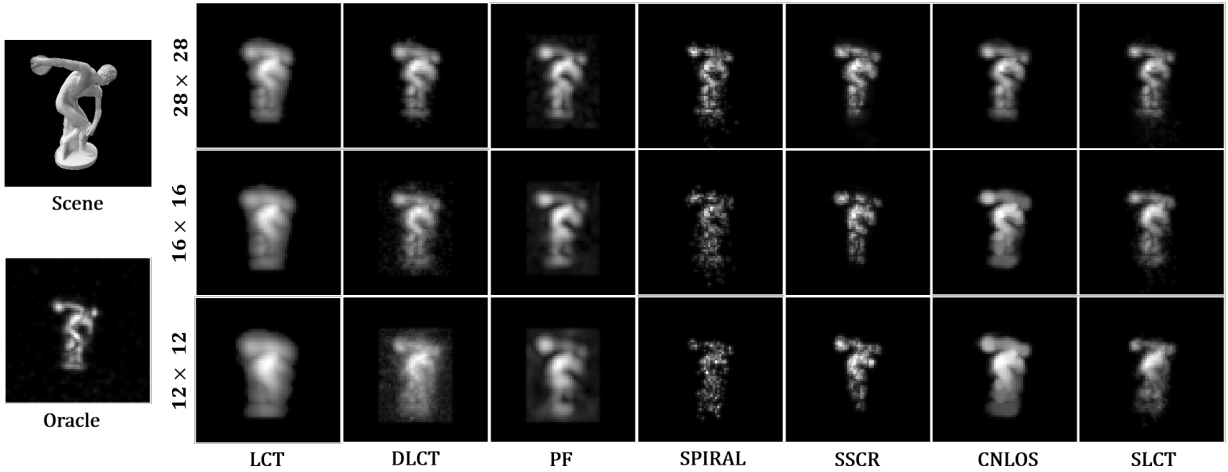


Fig. 9: Comparison results on ‘statue’ with exposure time of 60 min, where the oracle is obtained by PF using  $64 \times 64$  scanning points with exposure time of 180 min. The parameters of our methods are set as:  $\sigma = 7.5e - 6$ ,  $\lambda = 0.02$  ( $28 \times 28$ );  $\sigma = 8e - 6$ ,  $\lambda = 0.05$  ( $16 \times 16$ );  $\sigma = 1e - 5$ ,  $\lambda = 0.08$  ( $12 \times 12$ ).

TABLE I: Comparison w.r.t. different numbers of illumination points on the ‘statue’ with an exposure time of 60 min, where ‘R time’ and ‘T time’ represent reconstruction and total time (data acquisition and reconstruction) in seconds, respectively.

Methods	$28 \times 28$				$16 \times 16$				$12 \times 12$			
	PSNR $\uparrow$	SSIM $\uparrow$	Rtime $\downarrow$	Ttime $\downarrow$	PSNR $\uparrow$	SSIM $\uparrow$	Rtime $\downarrow$	Ttime $\downarrow$	PSNR $\uparrow$	SSIM $\uparrow$	Rtime $\downarrow$	Ttime $\downarrow$
LCT [17]	20.915	0.668	0.5	11.3	19.668	0.633	0.5	4.0	17.780	0.588	0.5	2.5
DLCT [24]	22.848	0.682	5.8	16.6	22.228	0.625	5.8	9.3	18.588	0.534	5.8	7.8
PF [18]	23.939	0.632	0.9	11.7	23.008	0.602	0.9	4.4	20.357	0.547	0.9	2.9
SPIRAL [31]	24.242	0.703	34.2	45.0	21.918	0.676	43.3	46.8	20.690	0.646	39.5	41.5
SSCR [35]	25.527	0.733	1469.5	1480.3	23.616	0.695	490.6	494.1	22.654	0.675	268.7	270.7
CNLOS [34]	25.318	0.711	15.2	26.0	23.006	0.688	15.2	18.7	20.849	0.669	15.2	17.2
<b>SLCT</b>	<b>25.813</b>	<b>0.738</b>	<b>5.4</b>	<b>16.2</b>	<b>24.304</b>	<b>0.710</b>	<b>5.4</b>	<b>8.9</b>	<b>22.969</b>	<b>0.682</b>	<b>5.4</b>	<b>7.4</b>

TABLE II: Comparison among different methods with various scanning points and exposure times on ‘dragon’, where time is recorded in seconds unless otherwise specified.

Methods	15sec $64 \times 64$				60min $28 \times 28$				60min $16 \times 16$			
	PSNR $\uparrow$	SSIM $\uparrow$	Rtime $\downarrow$	Ttime $\downarrow$	PSNR $\uparrow$	SSIM $\uparrow$	Rtime $\downarrow$	Ttime $\downarrow$	PSNR $\uparrow$	SSIM $\uparrow$	Rtime $\downarrow$	Ttime $\downarrow$
LCT [17]	18.238	0.416	0.5	0.7	19.462	0.711	0.5	11.3	16.041	0.477	0.5	4.0
DLCT [24]	20.367	0.488	5.8	6.0	19.725	0.424	5.8	16.6	15.055	0.331	5.8	9.3
PF [18]	19.225	0.453	0.9	1.1	20.110	0.641	0.9	11.7	18.108	0.474	0.9	4.4
SPIRAL [31]	21.408	0.791	30.5	30.7	20.506	0.771	27.7	38.5	19.639	0.742	24.9	28.4
SSCR [35]	21.749	0.838	> 40min	> 40min	18.760	0.781	978.9	989.7	18.236	0.774	408.1	411.6
CNLOS [34]	22.680	0.733	15.2	15.4	<b>22.227</b>	0.728	15.2	26.0	18.325	0.771	15.2	18.7
<b>SLCT</b>	<b>23.265</b>	<b>0.870</b>	<b>5.4</b>	<b>5.6</b>	22.119	<b>0.841</b>	<b>5.4</b>	<b>16.2</b>	<b>20.375</b>	<b>0.817</b>	<b>5.4</b>	<b>8.9</b>

comparisons highlight that geometric constraints on the object surface substantially enhance NLOS reconstruction quality.

### F. Comparison results on nonconfocal data

Finally, we evaluate our SLCT method on a nonconfocal dataset, comparing it with non-confocal solvers SSCR and CNLOS. Additionally, using the midpoint approximation method from [19], we convert non-confocal data to confocal data and compare our method with LCT, DLCT, PF, and SPIRAL. As shown in Fig. 12, our method consistently delivers the clearest and highest-resolution results across all three scanning setting.

At  $6 \times 6$  and  $4 \times 4$  scanning points, methods other than SSCR, CNLOS, and ours exhibit noticeable degradation. Even at a  $4 \times 4$  scanning points, our method achieves high-quality image reconstruction, outperforming other approaches.

### G. Complexity analysis

We theoretically compare the computational and memory complexities of various algorithms. For a reconstruction region with discrete voxel dimensions of  $N \times N \times N$ , and a visible wall sampled at  $N \times N$  points, the space complexity is  $O(N^3)$ , as the maximum data stored is the signal  $\tau$  or the reconstructed

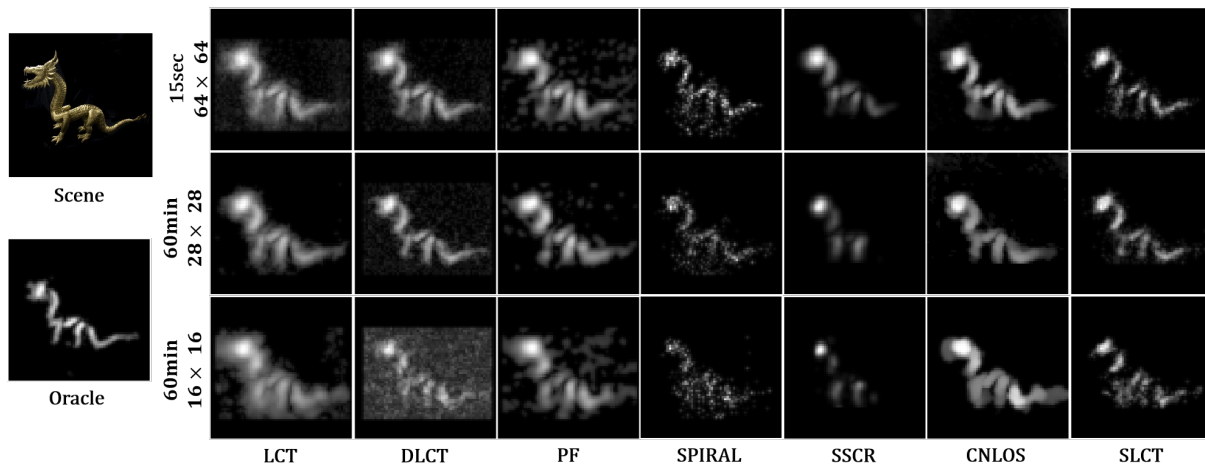


Fig. 10: Comparison of reconstruction results using different methods on ‘dragon’ with varying scanning points and exposure times. The oracle is obtained by PF using  $64 \times 64$  measurements of exposure time 180 min. The parameters of our methods are set as:  $\sigma = 8e - 6$ ,  $\lambda = 0.1$  (15sec,  $64 \times 64$ );  $\sigma = 8e - 6$ ,  $\lambda = 0.1$  (60min,  $28 \times 28$ );  $\sigma = 9.5e - 6$ ,  $\lambda = 0.35$  (60min,  $16 \times 16$ ).

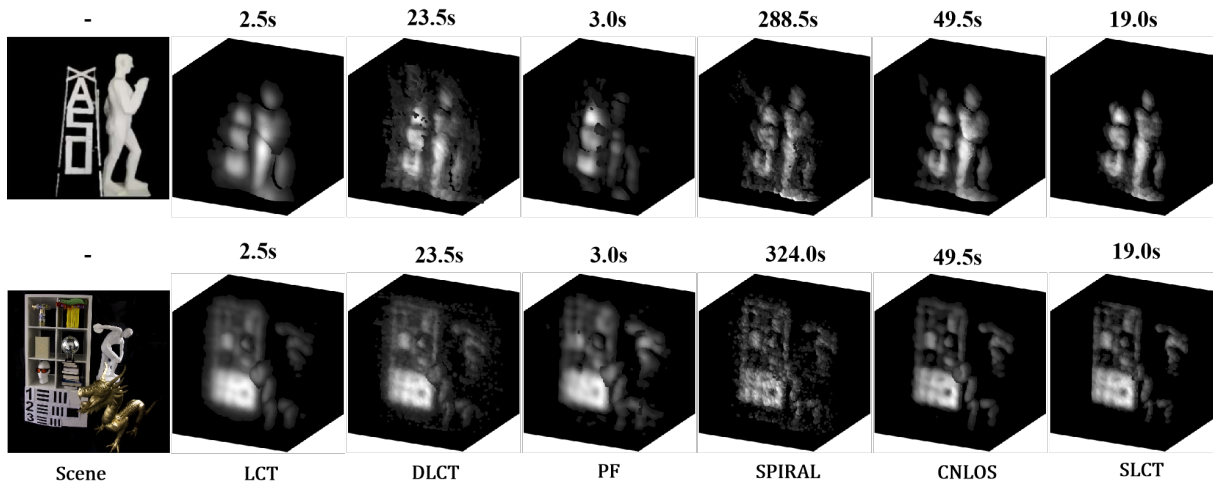


Fig. 11: Comparison results on ‘man letter’ and ‘teaser’ with  $16 \times 16$  scanning points and  $28 \times 28$  scanning points, respectively. The parameters of our methods are set as:  $\sigma = 8e - 6$ ,  $\lambda = 0.12$  (man letter);  $\sigma = 6.5e - 6$ ,  $\lambda = 0.1$  (teaser).

TABLE III: Performance evaluation of our SLCT on ‘outdoor’ and ‘dragon’ scene, where ‘S.Rec.’ denotes the sparse signal reconstruction module w.r.t. eq. (9), ‘S.Res.’ denotes the signal restoration module w.r.t. eq. (6), and ‘G.Con.’ denotes the geometric constraints on depth image  $D$  and albedo image  $I$ .

	Methods			outdoor		dragon	
	S.Rec.	S.Res.	G.Con.	PSNR $\uparrow$	SSIM $\uparrow$	PSNR $\uparrow$	SSIM $\uparrow$
I	✓	✗	✗	19.738	0.800	19.998	0.814
II	✓	✓	✗	21.260	0.794	20.363	0.762
III	✓	✓	✓	<b>21.348</b>	<b>0.815</b>	<b>20.375</b>	<b>0.817</b>

image  $u$ . Table IV summarizes the time complexity of different methods. Except for SSCR, all methods have a computational time complexity of  $O(N^3 \log N)$  for  $N \times N$  scanning points.

## VI. CONCLUSION AND DISCUSSION

In this paper, we introduced a geometric-constrained NLOS imaging reconstruction model that applies constraints on surface normals using the shape operator. Accurate normal reconstruction is crucial to capture the details and contours of the object. Our model enhanced object reconstruction accuracy through incorporating geometric constraints. Additionally, regularization on 2D depth and albedo maps significantly improved computational efficiency compared to volumetric albedo regularization. Experimental results demonstrated that the proposed method outperforms existing direct and iterative approaches in reconstruction quality under sparse illumination and low exposure conditions.

However, non-convex surfaces inherently introduce ambiguities, resulting in a many-to-one mapping between the actual geometry and its corresponding projection. This fundamentally challenges the uniqueness of the reconstruction process. A

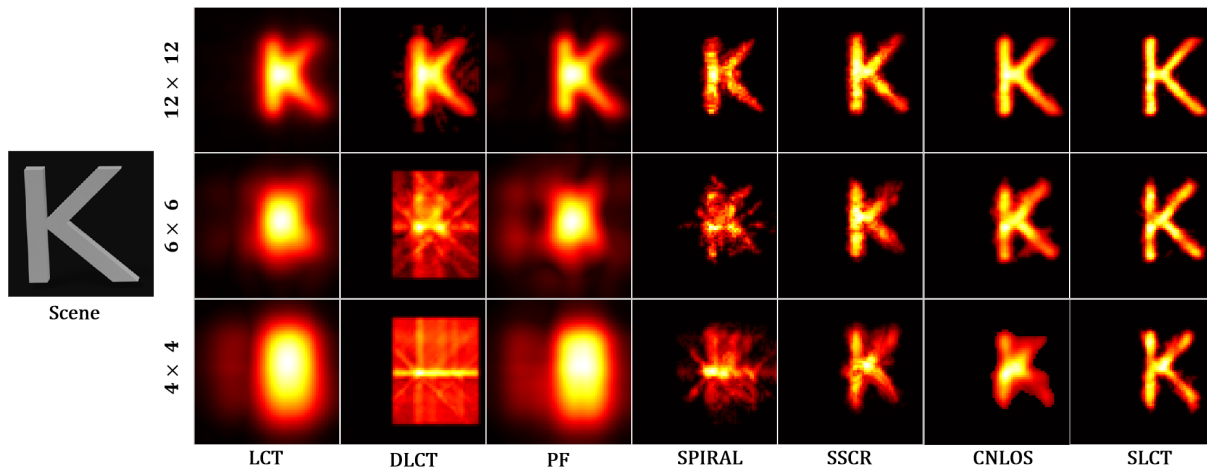


Fig. 12: Comparison on the nonconfocal dataset ‘K’ with 4×4, 6×6, and 12×12 scanning points is conducted using our method with the following parameters: for 12×12 scanning points,  $\sigma = 9 \times 10^{-6}$  and  $\lambda = 0.5$ ; for 6×6,  $\sigma = 9.5 \times 10^{-6}$  and  $\lambda = 0.5$ ; and for 4×4,  $\sigma = 10 \times 10^{-6}$  and  $\lambda = 0.5$ .

TABLE IV: Computational time complexity for a reconstruction region of  $N \times N \times N$  and scanning points of  $N \times N$ .

	Regularization					Data term	In total
	Lasso (3D)	Dictionary (3D)	Curvature (3D)	TV (2D)	Shape Operator (2D)		
LCT [17]	/	/	/	/	/	$O(N^3 \log N)$	$O(N^3 \log N)$
DLCT [24]	/	/	/	/	/	$O(N^3 \log N)$	$O(N^3 \log N)$
PF [18]	/	/	/	/	/	$O(N^3 \log N)$	$O(N^3 \log N)$
SPIRAL [31]	$O(N^3)$	/	/	/	/	$O(N^3 \log N)$	$O(N^3 \log N)$
SSCR [35]	$O(N^3)$	$O(N^3)$	/	/	/	$O(N^5)$	$O(N^5)$
CNLOS [34]	/	/	$O(N^3 \log N)$	/	/	$O(N^3 \log N)$	$O(N^3 \log N)$
SLCT	$O(N^3)$	/	/	$O(N^2 \log N)$	$O(N^2 \log N)$	$O(N^3 \log N)$	$O(N^3 \log N)$

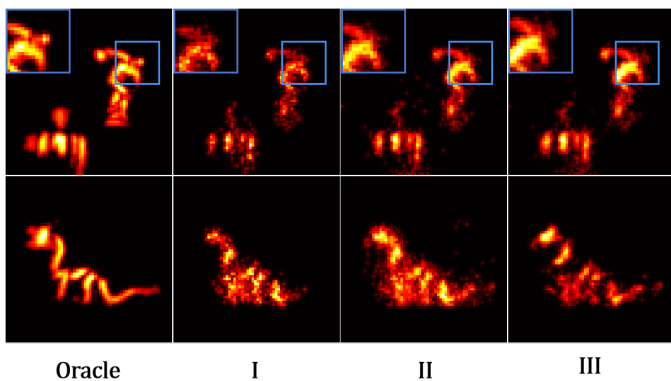


Fig. 13: Comparison on ‘outdoor’ (10 min) and ‘dragon’ (60 min) scenes with 28×28 and 16×16 scanning points, respectively. The two oracles are generated using the PF method with 64×64 measurements and exposure times of 50 min and 180 min.

potential solution to this problem is to leverage the conformal geometry to eliminate self-overlapping [49], [50], thereby improving the stability and reliability of the reconstruction. In future work, we aim to use conformal geometry to create a one-to-one mapping between the surface and two-dimensional depth and intensity maps, which can greatly facilitate higher-quality reconstructions for both traditional model-based and

deep learning-based approaches.

#### ACKNOWLEDGMENTS

The work is supported by the National Natural Science Foundation of China (NSFC 12071345). Yuping Duan is the corresponding author.

#### REFERENCES

- [1] D. Faccio, A. Velten, and G. Wetzstein, “Non-line-of-sight imaging,” *Nature Reviews Physics*, vol. 2, no. 6, pp. 318–327, 2020.
- [2] N. Scheiner, F. Kraus, F. Wei, B. Phan, F. Mannan, N. Appenrodt, W. Ritter, J. Dickmann, K. Dietmayer, B. Sick *et al.*, “Seeing around street corners: Non-line-of-sight detection and tracking in-the-wild using doppler radar,” in *Proceedings of the IEEE/CVF Conference on Computer Vision and Pattern Recognition*, 2020, pp. 2068–2077.
- [3] M. Isogawa, Y. Yuan, M. O’Toole, and K. M. Kitani, “Optical non-line-of-sight physics-based 3d human pose estimation,” in *2020 IEEE/CVF Conference on Computer Vision and Pattern Recognition, CVPR 2020, Seattle, WA, USA, June 13-19, 2020*, 2020, pp. 7011–7020.
- [4] W. Chen, F. Wei, K. N. Kutulakos, S. Rusinkiewicz, and F. Heide, “Learned feature embeddings for non-line-of-sight imaging and recognition,” *ACM Transactions on Graphics (ToG)*, vol. 39, no. 6, pp. 1–18, 2020.
- [5] J. Bertolotti, E. G. Van Putten, C. Blum, A. Lagendijk, W. L. Vos, and A. P. Mosk, “Non-invasive imaging through opaque scattering layers,” *Nature*, vol. 491, no. 7423, pp. 232–234, 2012.
- [6] O. Katz, P. Heidmann, M. Fink, and S. Gigan, “Non-invasive single-shot imaging through scattering layers and around corners via speckle correlations,” *Nature Photonics*, vol. 8, no. 10, pp. 784–790, 2014.
- [7] C. Saunders, R. Bose, J. Murray-Bruce, and V. K. Goyal, “Multi-depth computational periscopy with an ordinary camera,” in *ICASSP 2020-2020 IEEE International Conference on Acoustics, Speech and Signal Processing (ICASSP)*. IEEE, 2020, pp. 9299–9305.

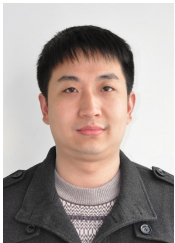
- [8] J. H. Nam, E. Brandt, S. Bauer, X. Liu, M. Renka, A. Tosi, E. Sifakis, and A. Velten, "Low-latency time-of-flight non-line-of-sight imaging at 5 frames per second," *Nature Communications*, vol. 12, no. 1, p. 6526, 2021.
- [9] C. Pei, A. Zhang, Y. Deng, F. Xu, J. Wu, D. U.-L. Li, H. Qiao, L. Fang, and Q. Dai, "Dynamic non-line-of-sight imaging system based on the optimization of point spread functions," *Optics Express*, vol. 29, no. 20, pp. 32 349–32 364, 2021.
- [10] R. Cao, F. De Goumoëns, B. Blochet, J. Xu, and C. Yang, "High-resolution non-line-of-sight imaging employing active focusing," *Nature Photonics*, vol. 16, no. 6, pp. 462–468, 2022.
- [11] M. Batarseh, S. Sukhov, Z. Shen, H. Gemar, R. Rezvani, and A. Dogariu, "Passive sensing around the corner using spatial coherence," *Nature Communications*, vol. 9, no. 1, p. 3629, 2018.
- [12] R. Geng, Y. Hu, Z. Lu, C. Yu, H. Li, H. Zhang, and Y. Chen, "Passive non-line-of-sight imaging using optimal transport," *IEEE Transactions on Image Processing*, vol. 31, pp. 110–124, 2021.
- [13] A. Kadambi, R. Whyte, A. Bhandari, L. Streeter, C. Barsi, A. Dorrington, and R. Raskar, "Coded time of flight cameras: sparse deconvolution to address multipath interference and recover time profiles," *ACM Transactions on Graphics (ToG)*, vol. 32, no. 6, pp. 1–10, 2013.
- [14] M. Buttafava, J. Zeman, A. Tosi, K. Eliceiri, and A. Velten, "Non-line-of-sight imaging using a time-gated single photon avalanche diode," *Optics Express*, vol. 23, no. 16, pp. 20 997–21 011, 2015.
- [15] V. Arellano, D. Gutierrez, and A. Jarabo, "Fast back-projection for non-line of sight reconstruction," in *ACM SIGGRAPH 2017 Posters*, 2017, pp. 1–2.
- [16] A. Velten, T. Willwacher, O. Gupta, A. Veeraraghavan, M. G. Bawendi, and R. Raskar, "Recovering three-dimensional shape around a corner using ultrafast time-of-flight imaging," *Nature Communications*, vol. 3, no. 1, p. 745, 2012.
- [17] M. O'Toole, D. B. Lindell, and G. Wetzstein, "Confocal non-line-of-sight imaging based on the light-cone transform," *Nature*, vol. 555, no. 7696, pp. 338–341, 2018.
- [18] X. Liu, S. Bauer, and A. Velten, "Phasor field diffraction based reconstruction for fast non-line-of-sight imaging systems," *Nature Communications*, vol. 11, no. 1, p. 1645, 2020.
- [19] D. B. Lindell, G. Wetzstein, and M. O'Toole, "Wave-based non-line-of-sight imaging using fast fk migration," *ACM Transactions on Graphics (ToG)*, vol. 38, no. 4, pp. 1–13, 2019.
- [20] C.-Y. Tsai, K. N. Kutulakos, S. G. Narasimhan, and A. C. Sankaranarayanan, "The geometry of first-returning photons for non-line-of-sight imaging," in *Proceedings of the IEEE Conference on Computer Vision and Pattern Recognition*, 2017, pp. 7216–7224.
- [21] F. Heide, M. O'Toole, K. Zang, D. B. Lindell, S. Diamond, and G. Wetzstein, "Non-line-of-sight imaging with partial occluders and surface normals," *ACM Transactions on Graphics (ToG)*, vol. 38, no. 3, pp. 1–10, 2019.
- [22] S. Xin, S. Nousias, K. N. Kutulakos, A. C. Sankaranarayanan, S. G. Narasimhan, and I. Gkioulekas, "A theory of fermat paths for non-line-of-sight shape reconstruction," in *Proceedings of the IEEE/CVF Conference on Computer Vision and Pattern Recognition*, 2019, pp. 6800–6809.
- [23] C.-Y. Tsai, A. C. Sankaranarayanan, and I. Gkioulekas, "Beyond volumetric albedo—a surface optimization framework for non-line-of-sight imaging," in *Proceedings of the IEEE/CVF Conference on Computer Vision and Pattern Recognition*, 2019, pp. 1545–1555.
- [24] S. I. Young, D. B. Lindell, B. Girod, D. Taubman, and G. Wetzstein, "Non-line-of-sight surface reconstruction using the directional light-cone transform," in *Proceedings of the IEEE/CVF Conference on Computer Vision and Pattern Recognition*, 2020, pp. 1407–1416.
- [25] Y. Fujimura, T. Kushida, T. Funatomi, and Y. Mukaigawa, "Nlos-neus: Non-line-of-sight neural implicit surface," in *Proceedings of the IEEE/CVF International Conference on Computer Vision*, 2023, pp. 10 532–10 541.
- [26] M. La Manna, F. Kine, E. Breitbach, J. Jackson, T. Sultan, and A. Velten, "Error backprojection algorithms for non-line-of-sight imaging," *IEEE Transactions on Pattern Analysis and Machine Intelligence*, vol. 41, no. 7, pp. 1615–1626, 2018.
- [27] Y. Ju, B. Shi, Y. Chen, H. Zhou, J. Dong, and K.-M. Lam, "Gr-psn: Learning to estimate surface normal and reconstruct photometric stereo images," *IEEE Transactions on Visualization and Computer Graphics*, vol. 30, no. 9, pp. 6192–6207, 2023.
- [28] C. Callenberg, Z. Shi, F. Heide, and M. B. Hullin, "Low-cost spad sensing for non-line-of-sight tracking, material classification and depth imaging," *ACM Transactions on Graphics (TOG)*, vol. 40, no. 4, pp. 1–12, 2021.
- [29] F. Heide, L. Xiao, W. Heidrich, and M. B. Hullin, "Diffuse mirrors: 3d reconstruction from diffuse indirect illumination using inexpensive time-of-flight sensors," in *Proceedings of the IEEE Conference on Computer Vision and Pattern Recognition*, 2014, pp. 3222–3229.
- [30] B. Ahn, A. Dave, A. Veeraraghavan, I. Gkioulekas, and A. C. Sankaranarayanan, "Convolutional approximations to the general non-line-of-sight imaging operator," in *Proceedings of the IEEE/CVF International Conference on Computer Vision*, 2019, pp. 7889–7899.
- [31] J.-T. Ye, X. Huang, Z.-P. Li, and F. Xu, "Compressed sensing for active non-line-of-sight imaging," *Optics Express*, vol. 29, no. 2, pp. 1749–1763, 2021.
- [32] X. Liu, J. Wang, Z. Li, Z. Shi, X. Fu, and L. Qiu, "Non-line-of-sight reconstruction with signal-object collaborative regularization," *Light: Science & Applications*, vol. 10, no. 1, p. 198, 2021.
- [33] D. Huang, Q. Chen, Z. Wei, and R. Chen, "Non-line-of-sight reconstruction via structure sparsity regularization," *Optics Letters*, vol. 48, no. 18, pp. 4881–4884, 2023.
- [34] R. Ding, J. Ye, Q. Gao, F. Xu, and Y. Duan, "Curvature regularization for non-line-of-sight imaging from under-sampled data," *IEEE Transactions on Pattern Analysis and Machine Intelligence*, vol. 46, no. 12, pp. 8474–8485, 2024.
- [35] X. Liu, J. Wang, L. Xiao, X. Fu, L. Qiu, and Z. Shi, "Few-shot non-line-of-sight imaging with signal-surface collaborative regularization," in *Proceedings of the IEEE/CVF Conference on Computer Vision and Pattern Recognition*, 2023, pp. 13 303–13 312.
- [36] X. Liu, S. Wei, W. Pu, X. Cai, Y. Wen, S. Guo, L. Kong, and X. Zhang, "Rm-cstv: An effective high-resolution method of non-line-of-sight millimeter-wave radar 3-d imaging," *National Science Open*, vol. 3, no. 5, p. 20230085, 2024.
- [37] J. Liu, Y. Zhou, X. Huang, Z.-P. Li, and F. Xu, "Photon-efficient non-line-of-sight imaging," *IEEE Transactions on Computational Imaging*, vol. 8, pp. 639–650, 2022.
- [38] S. Su, F. Heide, G. Wetzstein, and W. Heidrich, "Deep end-to-end time-of-flight imaging," in *Proceedings of the IEEE Conference on Computer Vision and Pattern Recognition*, 2018, pp. 6383–6392.
- [39] Y. Li, J. Peng, J. Ye, Y. Zhang, F. Xu, and Z. Xiong, "Nlost: Non-line-of-sight imaging with transformer," in *Proceedings of the IEEE/CVF Conference on Computer Vision and Pattern Recognition*, 2023, pp. 13 313–13 322.
- [40] S. Zhu, Y. M. Sua, T. Bu, and Y.-P. Huang, "Compressive non-line-of-sight imaging with deep learning," *Physical Review Applied*, vol. 19, no. 3, p. 034090, 2023.
- [41] X. Liu, J. Wang, L. Xiao, Z. Shi, X. Fu, and L. Qiu, "Non-line-of-sight imaging with arbitrary illumination and detection pattern," *Nature Communications*, vol. 14, no. 1, p. 3230, 2023.
- [42] J. Ye, Y. Hong, X. Su, X. Yuan, and F. Xu, "Plug-and-play algorithms for dynamic non-line-of-sight imaging," *ACM Transactions on Graphics*, vol. 43, no. 5, pp. 1–12, 2024.
- [43] S. Shen, Z. Wang, P. Liu, Z. Pan, R. Li, T. Gao, S. Li, and J. Yu, "Non-line-of-sight imaging via neural transient fields," *IEEE Transactions on Pattern Analysis and Machine Intelligence*, vol. 43, no. 7, pp. 2257–2268, 2021.
- [44] S. Osher, R. Fedkiw, and K. Piechor, "Level set methods and dynamic implicit surfaces," *Appl. Mech. Rev.*, vol. 57, no. 3, pp. B15–B15, 2004.
- [45] Q. Zhong, R. W. Liu, and Y. Duan, "Spatially adapted first and second order regularization for image reconstruction: from an image surface perspective," *Journal of Scientific Computing*, vol. 92, no. 2, p. 33, 2022.
- [46] A. Beck and M. Teboulle, "A fast iterative shrinkage-thresholding algorithm for linear inverse problems," *SIAM Journal on Imaging Sciences*, vol. 2, no. 1, pp. 183–202, 2009.
- [47] M. Galindo, J. Marco, M. O'Toole, G. Wetzstein, D. Gutierrez, and A. Jarabo, "A dataset for benchmarking time-resolved non-line-of-sight imaging," in *ACM SIGGRAPH 2019 Posters*, 2019, pp. 1–2.
- [48] J. Klein, M. Laurenzis, D. L. Michels, and M. B. Hullin, "A quantitative platform for non-line-of-sight imaging problems," in *British Machine Vision Conference*, 2018, p. 104.
- [49] L. M. Lui, W. Zeng, S.-T. Yau, and X. Gu, "Shape analysis of planar multiply-connected objects using conformal welding," *IEEE Transactions on Pattern Analysis and Machine Intelligence*, vol. 36, no. 7, pp. 1384–1401, 2013.
- [50] W. Chen, S. Sun, Y. Wang, N. Lei, C. Sadasivan, A. Tassiopoulos, S. Chen, H. Si, and X. Gu, "Robust surface remeshing based on conformal welding," in *Proceedings of the 2024 International Meshing Roundtable (IMR)*, 2024, pp. 0–0.



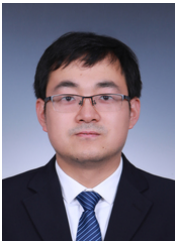
**Xueying Liu** is currently a master's candidate at the Center for Applied Mathematics of Tianjin University. Her research direction is non-line-of-sight imaging.



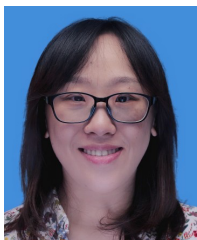
**Lianfang Wang** is currently pursuing a Ph.D. at Beijing Normal University. Her research focuses on deep learning-based methods applied to imaging fields, including computed tomography imaging and non-line-of-sight imaging.



**Jun Liu** received the B.S. degree in mathematics from the Hunan Normal University, China in 2004. He received the M.S. and Ph.D. degrees in computational mathematics from the Beijing Normal University (BNU), China, in 2008 and 2011 respectively. He is currently an associate professor at BNU. His research interests include variational, optimal transport and deep learning based image processing algorithms and their applications.



**Yong Wang** received the Ph.D. degree from the Institute of Physics, Chinese Academy of Sciences, Beijing, China, in 2009. He is currently an Associate Professor with the School of Physics, Nankai University, Tianjin, China. His research interests are theoretical and computational physics on materials and devices.



**Yuping Duan** is a full professor at the School of Mathematical Sciences of Beijing Normal University (BNU). Before joining BNU, she was a professor at Tianjin University in 2015 to 2023, and a research scientist at I2R, A\*STAR in 2012 to 2015. She received her Ph.D. from Nanyang Technological University in 2012. Her research interests are image processing and computer vision, variational methods, and deep learning methods.